2015

Impact of Local Winter Cooling on the Melt of Pine Island Glacier, Antarctica

P. St-Laurent
Old Dominion University, pstlaure@odu.edu

J. M. Klinck
Old Dominion University, jklinck@odu.edu

M. S. Dinniman
Old Dominion University, msd@ccpo.odu.edu

Original Publication Citation

St-Laurent, P., Klinck, J. M., & Dinniman, M. S. (2015). Impact of local winter cooling on the melt of Pine Island Glacier, Antarctica. *Journal of Geophysical Research: Oceans, 120*(10), 6718-6732. doi:10.1002/2015jc010709

AGU PUBLICATIONS

JGR

Journal of Geophysical Research: Oceans

RESEARCH ARTICLE

10.1002/2015JC010709

Key Points:
- Model study with an eddy-resolving ice-ocean model covering entire Amundsen Sea
- Winter cooling within polynyas is responsible for cold anomalies in September
- Coastal processes contribute to interannual variability of melt of glaciers

Supporting Information:
- Supporting Information S1
- Movie S1
- Movie S2

Correspondence to:
P. St-Laurent,
pierre@ccpo.odu.edu

Citation:
St-Laurent, P., J. M. Klinck, and M. S. Dinniman (2015), Impact of local winter cooling on the melt of Pine Island Glacier, Antarctica, *J. Geophys. Res. Oceans*, *120*, 6718–6732, doi:10.1002/2015JC010709.

Received 7 JAN 2015
Accepted 15 SEP 2015
Accepted article online 21 SEP 2015
Published online 15 OCT 2015

Impact of local winter cooling on the melt of Pine Island Glacier, Antarctica

P. St-Laurent[1], J. M. Klinck[1], and M. S. Dinniman[1]

[1]Center for Coastal Physical Oceanography, Old Dominion University, Norfolk, Virginia, USA

Abstract The rapid thinning of the ice shelves in the Amundsen Sea is generally attributed to basal melt driven by warm water originating from the continental slope. We examine the hypothesis that processes taking place on the continental shelf contribute significantly to the interannual variability of the ocean heat content and ice shelf melt rates. A numerical model is used to simulate the circulation of ocean heat and the melt of the ice shelves over the period 2006–2013. The fine model grid (grid spacing 1.5 km) explicitly resolves the coastal polynyas and mesoscale processes. The ocean heat content of the eastern continental shelf exhibits recurrent decreases around September with a magnitude that varies from year to year. The heat loss is primarily caused by surface heat fluxes along the eastern shore in areas of low ice concentration (polynyas). The cold winter water intrudes underneath the ice shelves and reduces the basal melt rates. Ocean temperatures upstream (i.e., at the shelf break) are largely constant over the year and cannot account for the cold events. The cooling is particularly marked in 2012 and its effect on the ocean heat content remains visible over the following years. The study suggests that ocean-atmosphere interactions in coastal polynyas contribute to the interannual variability of the melt of Pine Island Glacier.

1. Introduction

The ice shelves of the Amundsen and Bellingshausen Seas are thinning at rates as high as 6.8 m yr^{-1}, the fastest observed around Antarctica [*Pritchard et al*., 2012]. The unusually rapid thinning is generally attributed to basal melt driven by warm ocean water rather than iceberg calving or surface melt [*Rignot et al*., 2013]. The West Antarctic Ice Sheet (adjacent to the Amundsen and Bellingshausen Seas) is particularly vulnerable to this process as much of it is grounded below the sea level. This part of the continent experienced large recessions in the past 1 Myr that yielded substantial increases in the global sea level [*Naish et al*., 2009; *Pollard and DeConto*, 2009]. Recent studies suggest that most Amundsen Sea glaciers would be free of bed obstacles that could prevent further retreat [*Rignot et al*., 2014] and that early stage collapse may have begun [*Joughin et al*., 2014] assuming that present basal melt rates and warm ocean conditions are maintained in the future.

Ice volume budgets for the Amundsen embayment confirm that the ice flux changed considerably over the last decades. The discharge from Pine Island Glacier (PIG, see Figure 1) increased dramatically between 1994 and 2008 before stabilizing in 2009 [*Mouginot et al*., 2014, Figure 4a]. Although this variability may be related to glaciological processes (the grounding line reached the end of an ice plain around 2008), basal melt rates are known to be highly sensitive to ocean temperatures [*Holland et al*., 2008]. Observations collected between 1994 and 2012 indicate that the volume of warm modified Circumpolar Deep Water (mCDW) present on the continental shelf also increased between 1994 and 2009 and decreased afterward [*Dutrieux et al*., 2014].

One hypothesis to explain the interannual variability in mCDW is that large-scale atmospheric circulation patterns control the onshelf flux of ocean heat and consequently the melt of ice shelves in the Amundsen Sea (a "remote control") [*Thoma et al*., 2008; *Steig et al*., 2012]. Another hypothesis is that local processes (e.g., ocean heat loss in coastal polynyas) modulate the ocean heat content and thus the melt of ice shelves [e.g., *Gwyther et al*., 2014; *Khazendar et al*., 2013; *Padman et al*., 2012; *Holland et al*., 2010].

In this study, we examine the latter hypothesis using a 3-D ice shelf-sea ice-ocean coupled model. In contrast with earlier numerical studies, the fine grid of the model explicitly resolves the polynyas and mesoscale processes over the entire Amundsen Sea. The model is forced with winds from the Antarctic Mesoscale Prediction System (AMPS, 10–20 km grid spacing) that resolve the large glacial valleys surrounding the

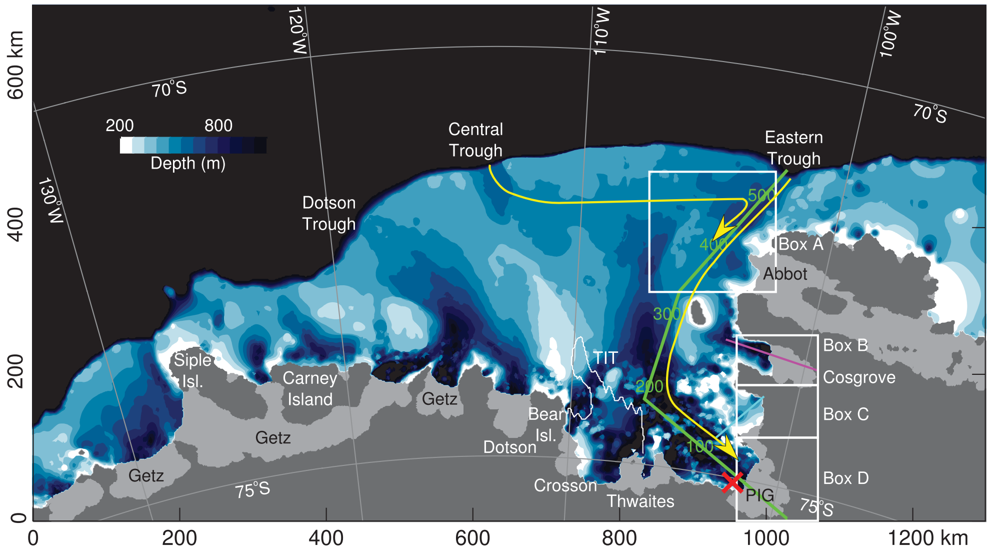

Figure 1. Model domain with the main ice shelves labeled. Color shading represents isobaths every 75 m. TIT is Thwaites Ice Tongue and PIG is Pine Island Glacier. The white boxes are the subdomains representing the eastern Amundsen Sea. The green line is the transect of Figure 2 with distance in kilometers from the ice shelf front (green numbers). The magenta and cyan lines represent the transect of Figures 6a–6d and 6e–6h, respectively. The yellow arrows are the pathways of CDW intrusions [*Nakayama et al.*, 2013]. The red symbol is the location of the model grid point for the temperature time series shown in Figure 11.

Amundsen Sea. The numerical experiments focus on the period 2006–2013 when the volume of mCDW present on the continental shelf started to decrease [*Dutrieux et al.*, 2014].

The next section describes the numerical model and the experiments of the study. Then, we present results that support the view that local processes contribute to modulating the ice shelf melt. The last section summarizes the main results and discusses their significance in the context of global sea level rise.

2. Method

To simulate the conditions in the Amundsen Sea we employ a 3-D sea ice-ocean coupled model (Regional Ocean Model System, ROMS version 3.4) [*Shchepetkin and McWilliams*, 2005; *Budgell*, 2005] thermodynamically coupled to static ice shelves (with the three-equation formulation of *Holland and Jenkins* [1999] and transfer coefficients that are function of the friction velocity; see *Dinniman et al.* [2011]). The model domain is 1400 $\times$ 735 km and covers the Amundsen Sea with a grid having a uniform horizontal spacing of 1.5 km (Figure 1). The fine grid is necessary to resolve the baroclinic Rossby radius (about 5 km on the continental shelf), to properly represent the small coastal polynyas $O(100\,\mathrm{km}^2)$ and the horizontal transport of ocean heat [e.g., *Årthun et al.*, 2013; *St-Laurent et al.*, 2013, Figure 13]. The domain geometry is from IBCSO [*Arndt et al.*, 2013, seafloor] and BEDMAP-2 [*Fretwell et al.*, 2013, ice shelves] and includes Cosgrove, Pine Island, Thwaites, Crosson, Dotson, and Getz ice shelves as well as most of Abbot (located at the edge of the domain, see Figure 1). These two data sets are considerably more detailed than other products [e.g., R-Topo 1.5; *Timmermann et al.*, 2010] but they also show significant differences in the shape of certain ice shelf cavities (notably Crosson and PIG). The vertical dimension is discretized with 20 topography-following (σ) levels with refinement near the surface. The ocean model uses constant diffusivities along the horizontal (biharmonic for momentum, 3×10^5 m^4 s^{-1}, and harmonic for scalars, 2 m^2 s^{-1}) and the *k*-profile parameterization in the vertical [*Large et al.*, 1994]. The sea ice component [*Budgell*, 2005; *Hedström*, 2009] combines the elastic-viscous-plastic rheology of *Hunke and Dukowicz* [1997] and thermodynamics [*Mellor and Kantha*, 1989] for one layer of ice and one layer of snow.

The numerical model is forced with daily averaged winds from AMPS [*Powers et al.*, 2012] having a changing horizontal grid spacing of 20 km (years 2006–2008), 15 km (2009–2012), and 10 km (2013). The annually averaged winds from these three periods are generally consistent despite the changes in grid spacing. The AMPS forecasts assimilate the data from three Automatic Weather Stations (AWS) installed in the Amundsen

Sea in early 2011. Winds are not available for the first 2 months of 2006 so they were taken from the same months in 2007. Comparisons between AMPS and ERA-Interim [*Dee et al*., 2011] for the other atmospheric fields show relatively small differences on monthly time scales. We thus use monthly averages from ERA-Interim covering the years 2006–2013 for all atmospheric fields other than winds. The model uses bulk formulas to calculate surface fluxes from the simulated ocean conditions and the prescribed surface atmospheric conditions [*Fairall et al*., 2003]. Tidal forcing is not included.

The lateral boundary conditions are restricted to climatologies in order to focus on the interannual variability generated locally. The lateral ocean boundary conditions are imposed as radiation-nudging [*Marchesiello et al*., 2001] to a monthly climatology assembled from 5 day state estimates of a 1/6° resolution sea ice-ocean model constrained by observations (Southern Ocean State Estimate, SOSE, data from 1 January 2008 to 31 December 2010) [see *Mazloff et al*., 2010]. Lateral boundary conditions for sea ice are from a monthly climatology assembled from daily sea ice concentration data from the Advanced Microwave Scanning Radiometer (AMSR-E, 12.5 km grid spacing, data from 1 January 2006 to 1 October 2011) [see *Cavalieri et al*., 2014]. Note that AMSR-E data became unavailable after October 2011.

The Thwaites Ice Tongue (TIT) is an extension of Thwaites ice shelf composed of landfast ice and partially grounded icebergs [e.g., *Tinto and Bell*, 2011]. It is a semipermanent feature of the basin [see *Scambos et al*., 2001] that acts as a barrier for the westward-drifting sea ice. In our simulations, the TIT is represented as a static extension of Thwaites ice shelf that blocks the passage of sea ice while allowing the ocean to freely circulate underneath it. The shape of the TIT varies slightly from year to year but the model requires its geometry to be constant. To circumvent this limitation, we pick the central year of the simulation (2009) and define the horizontal extent of the TIT as the area around Thwaites where the sea ice concentration from AMSR-E is $\geq$ 75% year round (Figure 1). The thickness of the TIT is poorly known and set to a uniform value in the model (1 m) for simplicity. The heat fluxes through the TIT are always small (section 7) since the TIT is treated as an extension of Thwaites ice shelf [see *Dinniman et al*., 2007].

The model starts from the SOSE fields on 1 January 2006 and is integrated in time for 16 years. The model atmospheric forcing covers the period 1 January 2006 to 31 December 2013 (8 years) and is repeated twice. The initial adjustment (spin-up) takes 5 years but for convenience we ignore the first 8 years altogether and focus our analysis on the second 8 years.

3. Model-Data Comparison

Field observations from the eastern side of the basin exhibit particularly warm water ($>$1°C) along a large glacial trough (Eastern Trough, Figure 1) [see *Dutrieux et al*., 2014]. Comparison between the model and data indicates that the model reproduces the intrusion of mCDW and the general thermal structure (Figure 2). The main deficiencies are an overly diffuse halo/thermocline, a warm bias of 0.5°C around 400 m in front of PIG, and a slight cold bias in the bottom layer. Bottom potential temperatures are $\sim$1.1°C in observations (Figure 2c) and $\sim$0.9°C in the model (Figure 2b; see also Figure 3b). Basal melt rates are most sensitive to bottom temperatures because the bulk of the melt takes place near the grounding lines (see supporting information).

Conditions on the western side of the Amundsen Sea are generally colder with maximum potential temperatures around 0.5°C [*Dutrieux et al*., 2014]. Comparison between the model and data collected along the ice shelf front (Figure 3) indicates that the model captures the west-east gradient in temperature. The thin thermocline (a regional proxy being the 2° above freezing isotherm) shoals from 600 m at Carney Island to 400 m near PIG. The main differences between the model and the data are a cold bias at depth in the eastern part of the domain (as noted above) and a warm bias west of Siple Island (thermocline 100 m too shallow). We attribute the warm bias to the boundary condition prescribed at the western edge of the model (the 2° isotherm is too shallow in SOSE).

The basal melt rates vary considerably among the main seven ice shelves of the basin (Table 1). The melt rates are largest underneath Thwaites ice shelf and PIG with values of 21 and 15 m yr^{-1}, respectively. The model reproduces the main regional differences but underestimates the melt of Crosson and Dotson Ice shelves and overestimates the melt of Cosgrove. Note that ice shelf melt rates are very sensitive to ocean temperatures [*Holland et al*., 2008] or ice shelf topography [*Little et al*., 2009] and that the model skill is better or comparable to previous modeling studies [e.g., *Timmermann et al*., 2012; *Schodlok et al*., 2012].

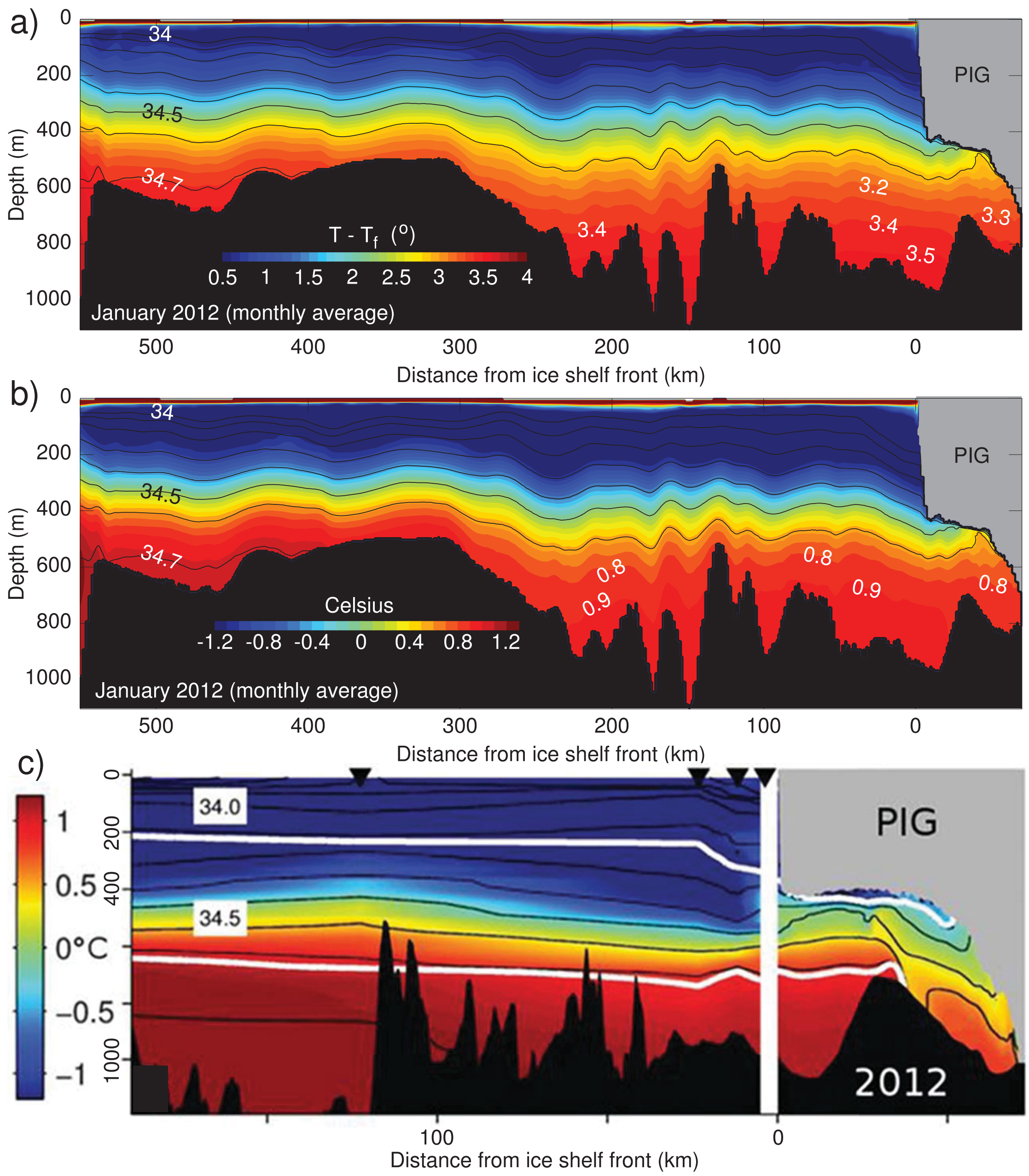

Figure 2. Temperature along the eastern trough (green line in Figure 1). (a) $T - T_f$ is the in situ temperature above the in situ freezing temperature. The black lines are isohalines every 0.1 psu. Results are averaged over January 2012. The model should be compared to *Jacobs et al.* [2011, Figure 2]. (b) Same as Figure 2a but for potential temperature. (c) Same as Figure 2b but from observations [*Dutrieux et al*., 2014, Figure 3b, used with permission]. The temperatures inside the cavity are taken from a numerical simulation [see *Dutrieux et al*., 2014]. Note the different horizontal scale in Figures 2b and 2c.

4. Interannual Variability of mCDW on the Continental Shelf

In this section, we use the model to investigate the variability in the heat content of the continental shelf. We specifically focus on four subdomains located within the Eastern Trough (boxes A–D, Figure 1). Box A is located at the entrance of the trough and represents the conditions upstream of the ice shelves. Boxes B to D represent the conditions in front of Cosgrove and PIG. The heat content within the subdomains is defined as the volume integration of the model potential temperature θ (in °C) averaged over blocks of 5 days. Note that this definition of the heat content allows for negative values wherever the water temperature is <0°C. We further divide each subdomain into an upper and a lower box representing the conditions above and

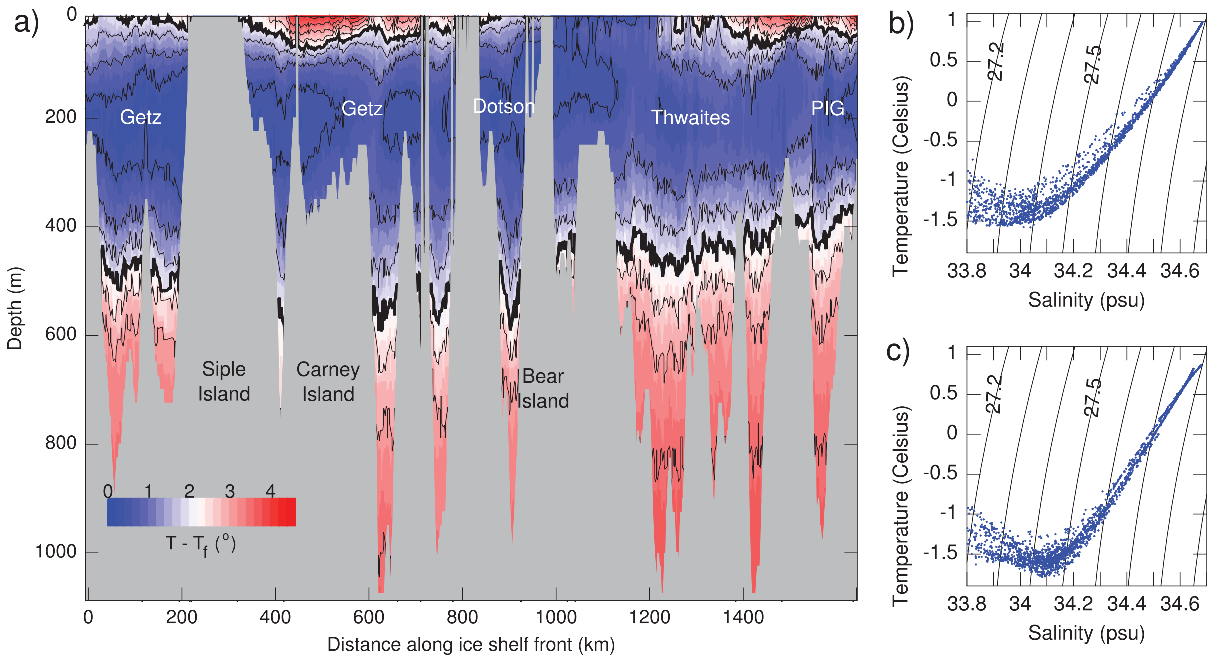

Figure 3. Simulated temperature along the ice shelf front (see Figure 1; results are averaged over January 2007). (a) $T-T_f$ is the in situ temperature above the in situ freezing temperature. The black contour lines highlight the isotherms (interval 0.5°, with 2° isotherm in bold). The model should be compared to *Jacobs et al.* [2012, Figure 2]. (b) Potential temperature-salinity diagram for the conditions east of Dotson Ice shelf. The black contour lines represent potential density (kg m^{-3}) referenced to the surface. (c) Same as Figure 3b but west of Dotson Ice shelf.

below 250 m, respectively. This depth horizon represents an arbitrary limit between the surface layers (that are heavily modified by surface fluxes) and the deeper layers.

The variability of the upper boxes is dominated by a large seasonal cycle in all the subdomains (Figures 4a and 4c). The heat content reaches a maximum in January–February and a minimum around November. The seasonality of the upper box is largely due to surface heat fluxes mediated by the seasonal sea ice cover (not shown). The heat content below 250 m follows a different evolution. Upstream of the ice shelves (box A, Figure 4b), the heat content gradually increases from 2006 to 2009 and decreases afterward (in qualitative agreement with the observations of *Dutrieux et al.* [2014]). The variability is considerably smaller than in the upper box. There is no obvious seasonality as peaks and troughs appear sometimes in summer and sometimes in winter.

In front of the ice shelves, the heat content of the lower box generally increases in 2006 and decreases in late 2012 (Figure 4d). The time series exhibit abrupt declines in September of years 2006, 2007, 2012, and 2013. These events are more pronounced at box B (Cosgrove) but are also visible at box C and D (see September 2007, 2012, and 2013). A decrease of 10×10^{11}°C m^3 is approximately equivalent to a 0.3°C decrease in the mean temperature of a box. We note that the overall variability is very different from the upstream box (A) and that boxes B, C, D tend to evolve together (Figures 4b and 4d). In the next section, we will focus on the origin of these cold events that affect Cosgrove and PIG.

Table 1. Model-Data Comparison for the Basal Melt Rates in Meters of Ice[a]

Reference	Abbot (m yr^{-1})	Cosgrove (m yr^{-1})	PIG (m yr^{-1})	Thwaites (m yr^{-1})	Crosson (m yr^{-1})	Dotson (m yr^{-1})	Getz (m yr^{-1})
Observed[b]	2.72 ± 0.7	3.74 ± 0.89	15.96 ± 2.38	15.22 ± 3.87		9.47 ± 0.83	4.09 ± 0.68
Observed[c]	1.85 ± 0.7	3.04 ± 0.8	17.61 ± 1	19.24 ± 1	12.9 ± 1	8.48 ± 0.7	4.67 ± 0.4
Model[d]	1.84 ± 0.1	6.97 ± 0.5	15.16 ± 1	21.02 ± 2	5.0 ± 0.2	4.07 ± 0.5	7.62 ± 1

[a]PIG is Pine Island Glacier.
[b]Years 2007–2009 [*Depoorter et al.*, 2013]. Crosson and Dotson are combined.
[c]Years 2007–2008 [*Rignot et al.*, 2013].
[d]Years 2007–2008. The ± represents the standard deviation of annually averaged values during the period 2006–2013.

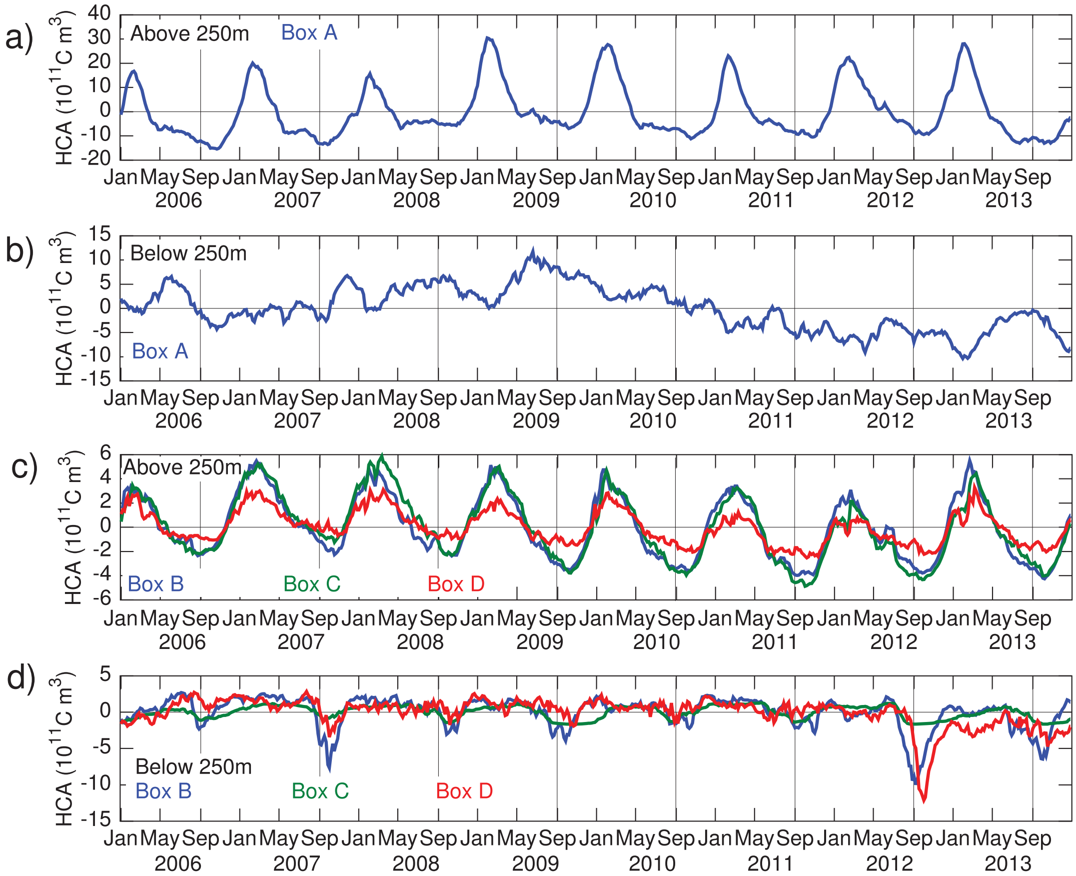

Figure 4. Heat content anomalies (HCAs) within subdomains of the eastern Amundsen Sea (box A–D, see Figure 1). The horizontal black line represents the mean value of the time series. (a) Heat content for the upper 250 m of box A. (b) Same as Figure 4a but for 250 m to the bottom. (c) Same as Figure 4a but for boxes B–D. (d) Same as Figure 4b but for boxes B–D.

5. Formation and Circulation of the Cold Anomalies

We investigate the origin of the cold anomalies by examining the ocean temperature and circulation in the months prior to September. For this purpose, we create a monthly climatology of the model results for the years 2006–2013. We specifically focus on the conditions at depth (250 m) since they are closer to the conditions underneath the ice shelves.

The month of June is characterized by relatively warm temperatures (>-0.3°C over the eastern trough) from the shelf break to PIG (Figure 5a). The flow is eastward at the shelf break and becomes southward within the eastern trough. The streamlines converge in front of PIG to form a clockwise gyre [e.g., *Thurnherr et al.*, 2014]. In the following months, the conditions at the shelf break stay relatively constant while the temperature along the coast becomes gradually cooler (Figures 5b–5d). The cooling is particularly vigorous in front of Cosgrove Ice Shelf and between Cosgrove and PIG (box C) with temperatures reaching -1.9°C at the coast (Figures 5b–5d). The streamlines indicate that some of this cold water is transported southward and joins with the clockwise gyre located in front of PIG. In October, the temperatures start to increase again along the eastern shore (Figures 5e and 5f).

The sequence of events shown in Figure 5 takes place every year but with different magnitude. The cooling is most apparent in September 2006, 2007, 2012, and 2013 (Figure 4d). The recurrence of the phenomenon is illustrated in two movies (see "supporting information") showing the heat content below 250 m and the temperature at 375 m depth, respectively. This depth horizon corresponds to the highest instrument on most moorings deployed in the Amundsen Sea.

We examine the formation of the cold anomalies in further detail with two transects located in front of Cosgrove ice shelf and between Cosgrove and PIG (magenta and cyan lines in Figure 1, respectively). In both

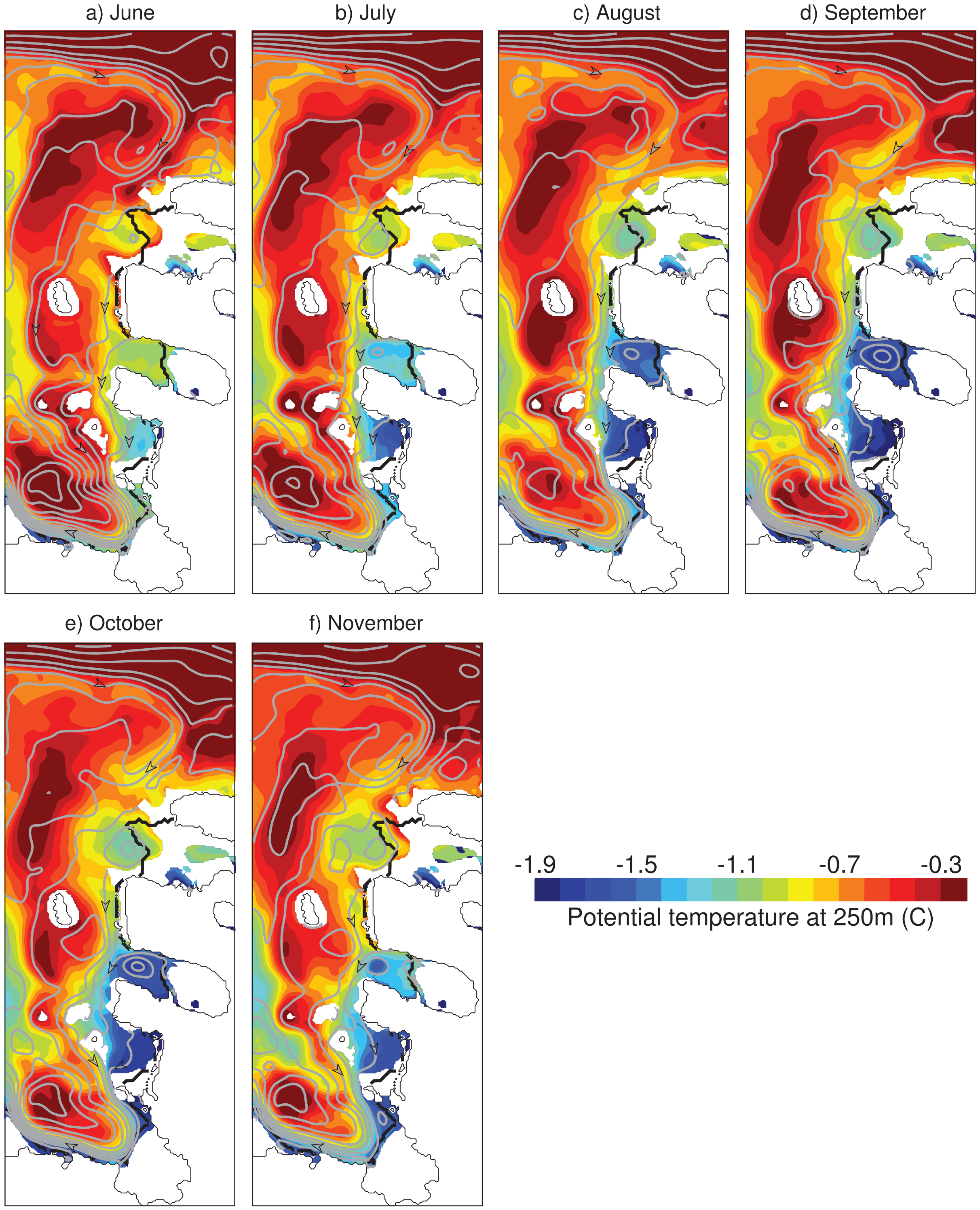

Figure 5. Formation and circulation of the cold anomalies (monthly climatology for years 2006–2013). The shading is the potential temperature at 250 m. The streamlines represent the mean ocean circulation at the same depth (interval 500 $m^2\ s^{-1}$). Areas that are land or ice shelf at 250 m are masked with solid white. The thick (thin) black line is the ice shelf front (grounding line).

cases, near-freezing water appears around June at the surface near the ice shelf front/coastline (Figures 6a and 6e). The cold water mass expands vertically and horizontally over the following months (Figures 6a–6h). By September, the $-1°C$ isotherm reaches the sea floor along the cyan transect (500 m depth, Figure 6h).

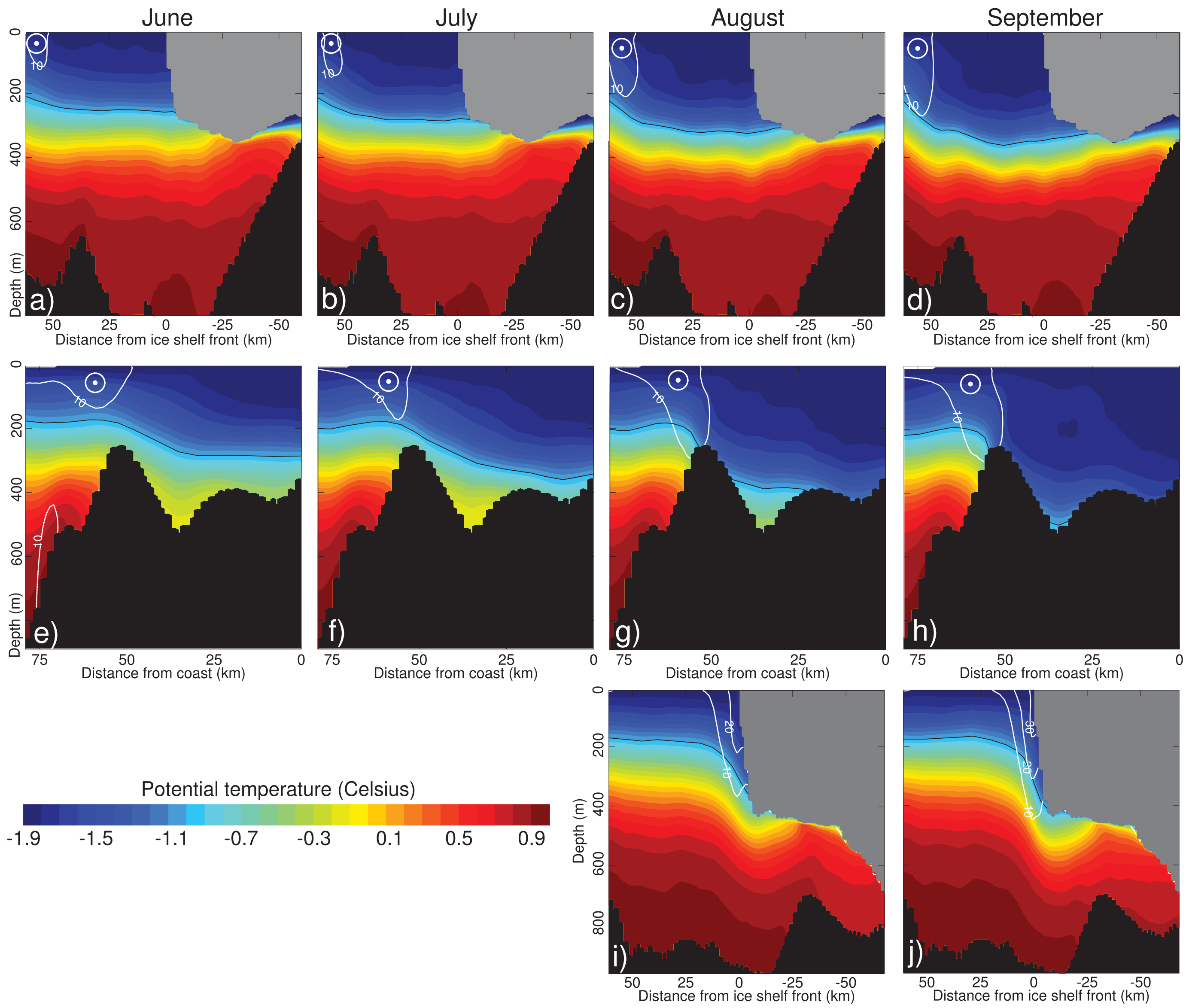

Figure 6. (a–d) Cooling in front of Cosgrove ice shelf, (e–h) between Cosgrove and Pine Island Glacier, and (i and j) in front of PIG. See Figure 1 for the location of the transects (magenta, cyan, and green lines, respectively). The black contour line is the -1°C isotherm. The white contour lines represent the flow perpendicular to the transect (positive/southward out of page; isolines of 10, 20, and 30 cm s^{-1} are shown). The southward coastal current is indicated by the symbol ⊙.

The results from these two transects are suggestive of large surface heat loss and cold water formation in front of Cosgrove and along the coastlines of box C.

The cold water mass expands sufficiently far offshore to affect the transport of heat within the southward coastal current (Figures 6d and 6h) that leads to the clockwise gyre of Pine Island Bay (Figure 5). This sequence of events, from the formation of cold water inside boxes B–C to its advection within the gyre, is represented in the two movies in "supporting information." The southward propagation of the cold anomaly is also represented by Hovmöller diagrams in supporting information. The signal propagates along the coast at a speed varying between 8 and 15 cm s^{-1}.

The passage of the cold anomaly in front of PIG is accompanied by a deepening of the isotherms between August and September (Figures 6i and 6j). The -1°C isotherm reaches down to 400 m in September which is sufficiently deep for the cold anomaly to affect the basal melt rates. Note that the strongly sheared and surface-intensified flow at the ice shelf front contributes to deepening the isotherms through the thermal wind relationship. The characteristics of the flow (speed $O(25\,\mathrm{cm\ s^{-1}})$ near the surface, decreasing to $\sim$0 at $\sim$550 m, Figures 6i and 6j) are in broad agreement with the observations of *Thurnherr et al*. [2014, Figure 6].

6. Heat Budget for the Coast of the Eastern Amundsen Sea

We examine the cause of the annual cooling occurring along the coastlines (e.g., Figures 5 and 6) by considering the heat budget of the boxes defined in Figure 1:

$$\frac{\partial}{\partial t}\mathcal{H}_{\mathrm{box}}(t) = S(t) + B(t) + I(t) + R(t), \tag{1}$$

where $\mathcal{H}_{\mathrm{box}}$ is a volume integration of the model potential temperature (bottom to surface), S is the net surface heat flux, B represents the net horizontal heat transport across the lateral boundaries of a box, and I is the heat flux at the ice shelf-ocean interface (where the box is bounded by an ice shelf). The budget represented in equation (1) is constructed from 5 day averages of each term in the temperature equation (time-derivative, horizontal and vertical advection, horizontal and vertical diffusion). The averaged fields are interpolated from the original topography-following grid to the boxes of Figure 1. A residual term $R(t)$ is added to equation (1) to represent the errors arising from the interpolation and from horizontal diffusion of heat (neglected in equation (1); the horizontal diffusivity is only 2 $\mathrm{m^2\ s^{-1}}$).

The cooling occurring in boxes B and C (Figures 5 and 6a–6h) is represented by large negative values for $\partial H/\partial t$ from March to October (Figures 7a and 7b). In both boxes, the negative $\partial H/\partial t$ is primarily due to the surface heat fluxes S. This term remains significant during the period of heavy sea ice cover (austral winter) which suggests the presence of polynyas along the coast (see next section). The next term in importance is the lateral transport of heat (B) that is generally positive and equivalent to an influx of warm water and/or an outflow of cold water. This term fluctuates over the year with the ocean circulation but it generally increases from August to November as the cold winter water produced in these boxes is gradually replaced by warmer water (Figure 5). The other terms of the budget (I, R) are relatively small and play a secondary role in the seasonal cycle (Figures 7a and 7b).

The heat budget for box D is qualitatively different than those of boxes B and C. The surface heat fluxes (S) are still significant but have a secondary effect on the seasonal cycle. The budget is dominated by the lateral heat transport (B) and by heat loss to the ice shelf (PIG, I). The heat transport decreases by $\sim$33% between August and September and leads to a similar decrease in ice shelf melt (I; in agreement with Figures 6i and 6j). In the next section, we will examine how the sea ice cover allows for the large surface heat loss and cooling along the eastern shore of the Amundsen Sea.

7. Heat Loss Within Polynyas

Winter-time surface heat loss is normally mediated by sea ice that acts as a thermal insulator. Satellite images reveal, however, recurrent areas of open water (polynyas) along the eastern shore of the Amundsen Sea during winter [*Mankoff et al*., 2012, Figure 5; *Scambos et al*., 2001]. The polynyas are represented in the model by ice concentrations approaching zero and correspondingly large surface heat fluxes.

The general distribution of sea ice simulated by the model is compared to satellite observations in Figure 8 (AMSR-E and SSM/I, Special Sensor Microwave Imager). The sea ice concentrations from SSM/I use the NASA Team (NT) algorithm on a 25 km grid [*Cavalieri et al*., 2015]. The sea ice concentrations from AMSR-E use the Enhanced NASA Team (NT2) algorithm on a 12.5 km grid [*Cavalieri et al*., 2014]. Both satellite data sets are gridded by summing and averaging the observational points whose center fall within a grid cell ("drop-in-bucket" method). A comparative study involving 21,600 ship-based observations around Antarctica [*Beitsch et al*., 2015] shows that SSM/I with the NT algorithm underestimates sea ice concentrations by 13.9% during winter. AMSR-E with the NT2 algorithm overestimates concentrations by 4.7% during the same period.

The model and the two satellite estimates exhibit relatively low ice concentrations in front of Abbot, Cosgrove, and PIG (Figure 8). This "band" of low ice concentration is 10–50 km wide, or only a few grid points of the satellite data. A large polynya is also apparent on the lee side of the Thwaites Ice Tongue (the Amundsen Sea Polynya). This qualitative agreement between model and data suggests that the simulated

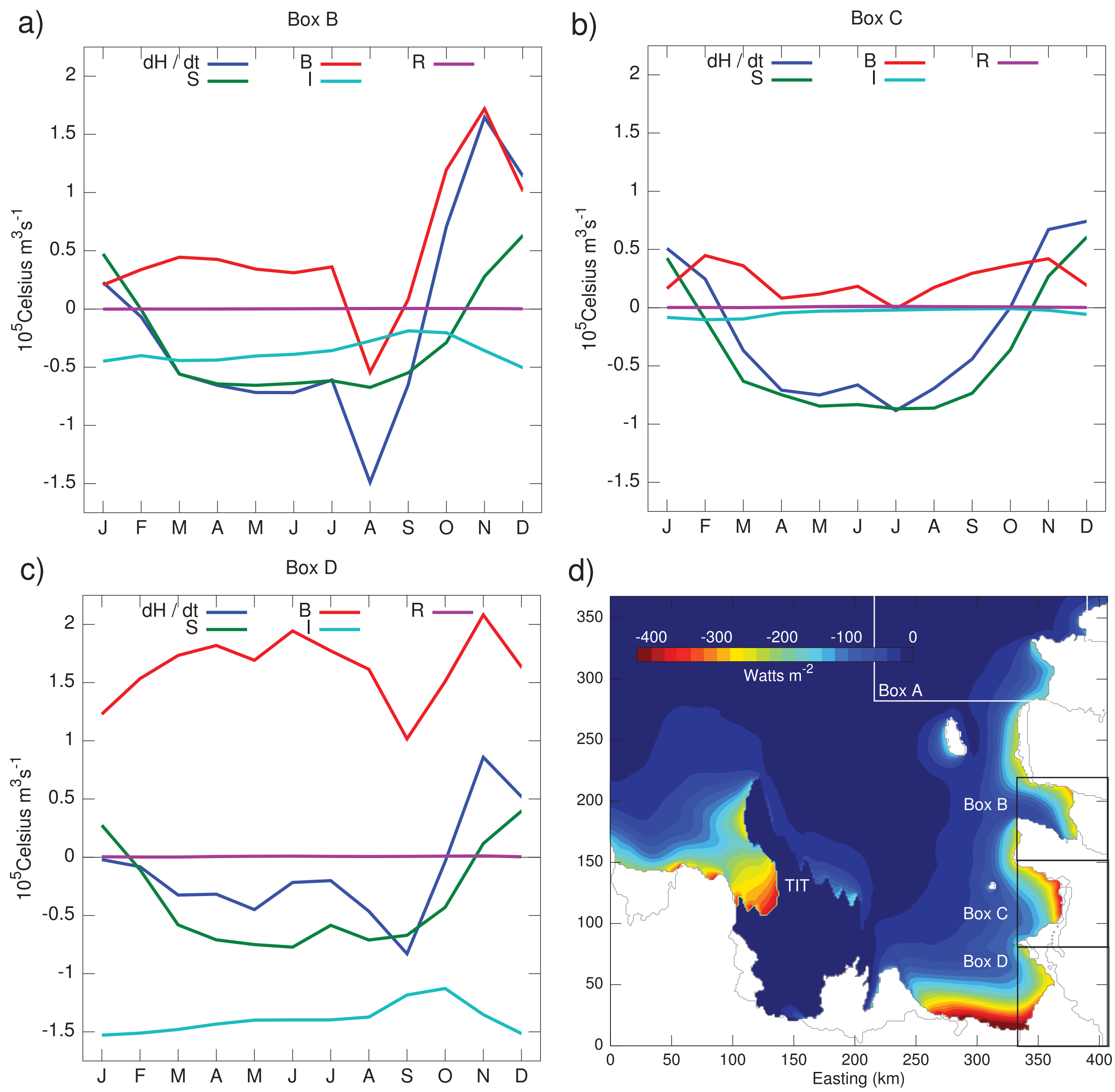

Figure 7. Seasonal heat budget along the eastern shore of the Amundsen Sea (equation (1)). The seasonal cycle corresponds to a monthly average of years 2006–2013. (a–c) Budget for box B, C, and D (respectively; see Figure 1). The budget is for the entire water column (bottom to surface). (d) Net heat flux at the surface of the ocean (<0 where the ocean loses heat) during July–August–September. The spatial distribution should be compared to Figure 8a. TIT is Thwaites Ice Tongue. The black contour line is the grounding line.

ice cover is reasonably realistic. We note however that the three figures differ in absolute numbers. SSM/I concentrations are consistently lower than AMSR-E (by 10–15%). These large differences are consistent with the biases reported by *Beitsch et al.* [2015]. The model is similar to AMSR-E away from the shores but closer to SSMI along the coasts. A more quantitative model-data comparison is further hindered by obvious differences in the shape of the coastlines and by artifacts from the "bucket" averaging [especially in SSM/I; e.g., *Martin et al.*, 2004].

The general distribution of sea ice plays a critical role in the heat budget of the model. The loss of heat from the ocean surface is effectively zero except within the areas of low ice concentrations described previously (Figure 7d). The polynyas allow a year-long exchange of heat between the ocean and the atmosphere inside box B and C (Figures 7a and 7b). The surface heat fluxes are responsible for the cold surface winter water that is subsequently transported toward PIG. In the next section, we examine the effect of the cold anomalies on the melt of PIG.

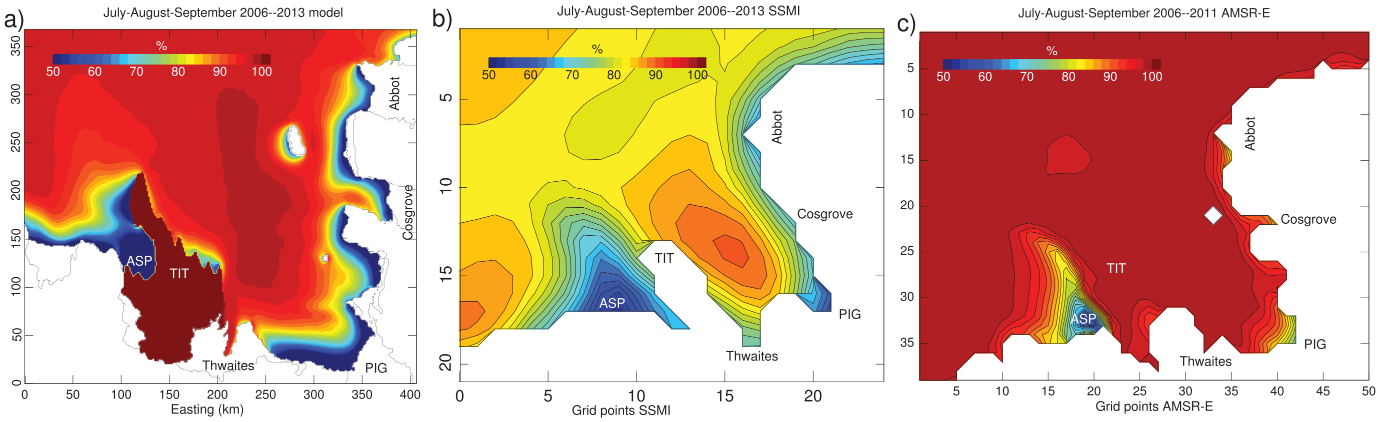

Figure 8. Average sea ice concentration during winter (July–August–September). (a) Modeled concentration for years 2006–2013. (b) Same as Figure 8a but from SSMI. (c) Same as Figure 8a but from AMSR-E and for years 2006–2011. ASP is Amundsen Sea Polynya, TIT is Thwaites Ice Tongue, and PIG is Pine Island Glacier.

8. Effect of the Cold Anomalies on Pine Island Glacier

The impact of the cold events on PIG is examined in Figure 9. We specifically focus on a potential density surface positioned approximately 20 m below the ice shelf (1027.525 kg m^{-3}). The ocean conditions prior to September are characterized by relatively warm temperatures underneath the ice shelf (>-0.5°C) and a vigorous outflow on the western side of the cavity (Figure 9a, in agreement with the observations of *Thurnherr et al*. [2014]). In September, the cold anomaly appears to propagate along the coast and within the southward current (described in section 5). It intrudes underneath PIG from its northern side and causes a temperature decrease of ~ -0.3°C in the northern half of the ice shelf cavity (Figure 9b). This cooling leads to a $\sim$20% decrease in the ice shelf melt rate between August and October (Figure 7c). Some of the cold water does not enter the ice shelf cavity and circulates along the ice shelf front before continuing westward (Figures 6i and 6j).

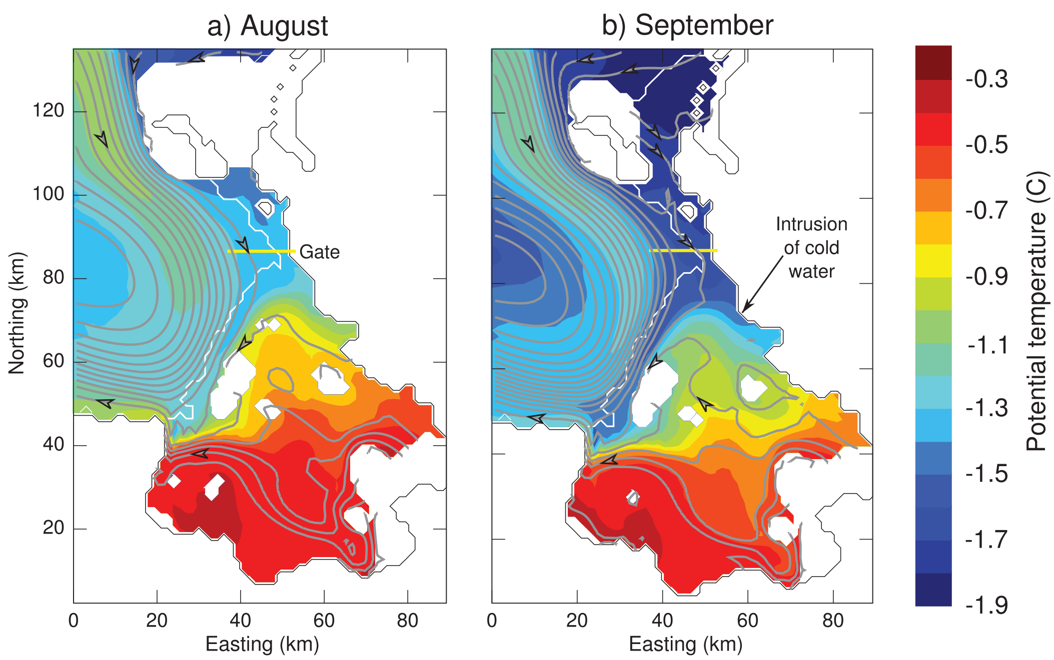

Figure 9. Intrusion of cold winter water inside the ice shelf cavity of Pine Island Glacier. (a) Model potential temperature (shading) and ocean circulation (streamlines, interval 250 m^2 s^{-1}) on a density surface (1027.525 kg m^{-3}). The fields are averaged over August 2006–2013. The black (white) line is the grounding line (ice shelf front). The yellow line is the gate used in Figure 10d. Areas where the isopycnal intersects the sea floor/ice shelf are in solid white. (b) Same as Figure 9a but for September.

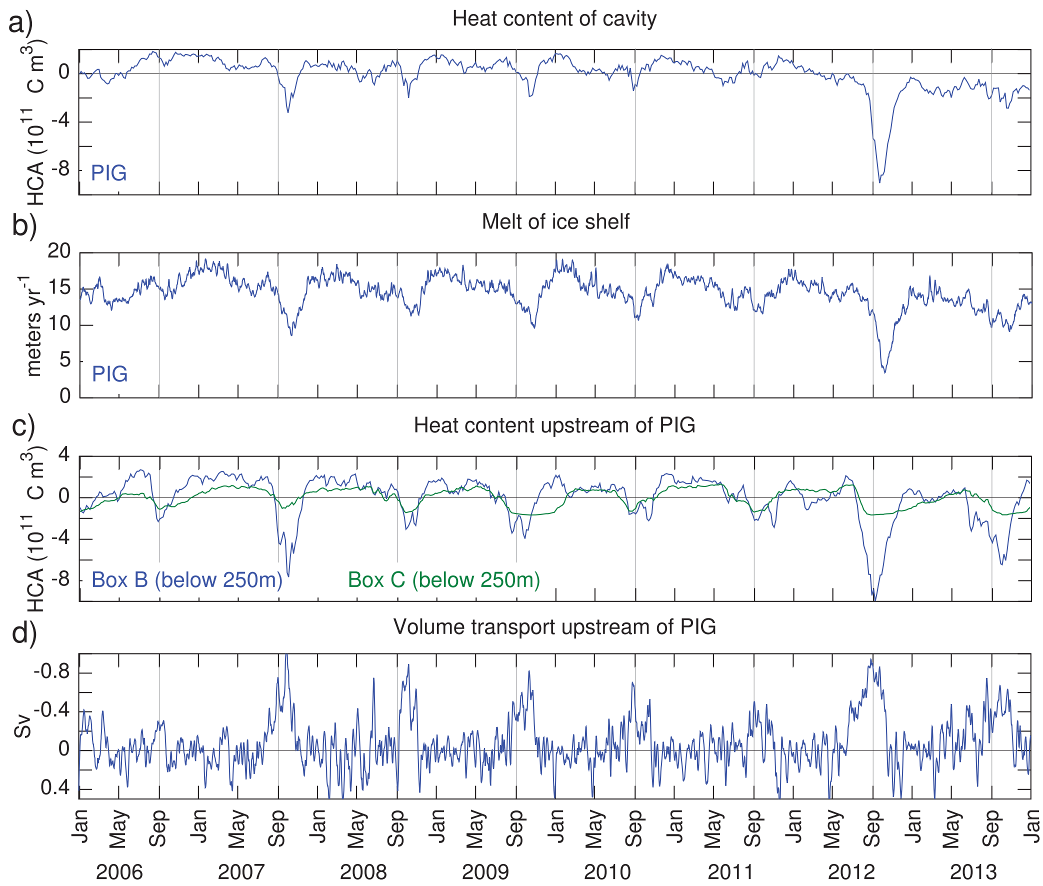

Figure 10. Heat content and melt of Pine Island Glacier (PIG). (a) Heat content based on potential temperature integrated over the ice shelf cavity. The mean value has been subtracted from the time series. HCA is Heat Content Anomaly. (b) Basal melt rate of the ice shelf. (c) Same as Figure 10a but for boxes B and C and depths greater than 250 m. (d) Volume transport across a gate located upstream of PIG (see Figure 9; 1 Sv$=10^6$ m^3 s^{-1}). The transport is negative southward. The time series in Figures 10b and 10d were smoothed with a 10 days low-pass filter.

This seasonal cooling occurs with a different magnitude over the years. The heat content of the ice shelf cavity (defined as in section 4 but with the volume integration limited to the cavity) shows small changes in September of years 2006 and 2011, and large decreases in 2007 and 2012 (Figure 10a). The cooling of September 2012 corresponds to a 35% decrease in the heat content of the cavity. The basal melt of the ice shelf closely follows the heat content and drops from 15 to 4 m yr^{-1} in this particular year (Figure 10b). The heat content partially recovers over the next 4 months but remains $\sim$10% lower than in the previous years, indicating that the cold events can have a lasting effect on the heat content and melt rates. The cold anomaly of September 2012 can be seen down to 600 m depth downstream of PIG (Figure 11). Abnormally cold temperatures remain visible at 300 m depth until May 2013.

Mooring data and numerical simulations covering longer periods of time will be required to fully understand the interannual variability of ice shelf melt rates in the Amundsen Sea. We can nevertheless use the present model results for a preliminary investigation. The variations in the heat content of PIG/box D are primarily driven by the lateral transport of heat (Figure 7c) which in turn depends on the heat content upstream and the ocean circulation. We thus define for our purpose the "heat content upstream of PIG" as the heat content below 250 m in boxes B–C, and the "volume transport upstream of PIG" as the depth-integrated flow across a gate positioned north of PIG (see Figure 9).

Interannual variations in the heat content upstream seem to explain some of the variations in PIG's heat content (compare Figures 10a and 10c) but certain discrepancies are apparent. The large heat loss in box B in September 2006 has no counterpart in PIG's heat content time series (Figures 10a and 10c). We suggest that such discrepancies could be caused by interannual variations in the ocean circulation. The transport

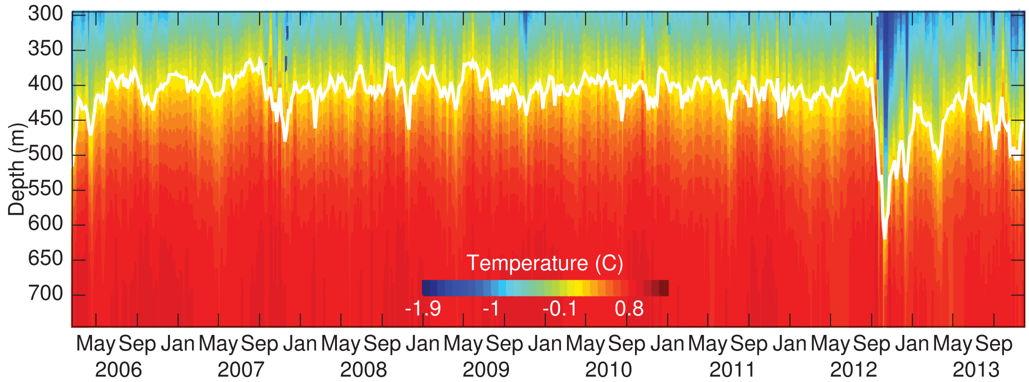

Figure 11. Model potential temperature downstream of Pine Island Glacier (75.055°S, 102.154°W; see Figure 1). The white contour line is the 0°C isotherm.

across the gate is relatively weak in September 2006 (Figure 10d) which would effectively prevent the cold water from reaching the ice shelf cavity. Additional in situ observations will be required to confirm or invalidate the model results.

9. Discussion and Summary

Field observations from the last 20 years describe the warming and subsequent cooling of the water on the continental shelf of the Amundsen Sea [*Dutrieux et al.*, 2014]. The variability is often attributed to the large-scale atmospheric circulation influencing the onshelf flux of heat [*Thoma et al.*, 2008; *Steig et al.*, 2012]. Additional observations are required however to confirm that this mechanism is the sole control over the melt of the ice shelves [e.g., *Wåhlin et al.*, 2013]. Our study suggests that local processes (surface heat loss in coastal polynyas) also modulate the heat content of the shelf and have a direct impact on ice shelf melt rates. Future modeling studies that aim to compare these two drivers should cover the entire range of variability at the shelf break and also resolve the coastal polynyas.

The importance of surface heat loss in coastal polynyas was highlighted in studies of Totten Glacier (another fast-melting glacier in Eastern Antarctica, *Khazendar et al*. [2013] and *Gwyther et al*. [2014]) and in the Bellingshausen Sea [*Padman et al*., 2012; *Holland et al*., 2010]. Such small-scale coastal processes represent a formidable obstacle for realistic projections of future ice sheet mass balance and global sea level rise. The Pine Island Glacier polynya cannot be represented explicitly in state-of-the-art climate models whose grid spacing is $O(10\,\text{km})$ and larger. Similarly, Antarctic ice sheet models often assume idealized ocean forcing and lack the ocean-atmosphere interactions described in this study [e.g., *Nowicki et al*., 2013]. A final caveat concerns the topography of the ice shelf cavities that changes over time and is not always properly constrained [see *Fretwell et al*., 2013].

Acknowledgments
This research was supported by the National Science Foundation under grant OCE-0927797. The data for this study are available upon request to the corresponding author (Pierre St-Laurent, pierre@ccpo.odu.edu). The authors are grateful for the helpful suggestions provided by the reviewers. AMPS data were provided by Ohio State University.

References

Arndt, J. E., et al. (2013), The International Bathymetric Chart of the Southern Ocean (IBCSO) Version 1.0—A new bathymetric compilation covering circum-Antarctic waters, *Geophys. Res. Lett.*, *40*, 3111–3117, doi:10.1002/grl.50413.

Årthun, M., P. Holland, and K. W. Nicholls (2013), Eddy-driven exchange between the open ocean and a sub-ice shelf cavity, *J. Phys. Oceanogr.*, *43*(11), 2372–2387, doi:10.1175/JPO-D-13-0137.1.

Beitsch, A., S. Kern, and L. Kaleschke (2015), Comparison of SSM/I and AMSR-E sea ice concentrations with ASPeCt ship observations around Antarctica, *IEEE Trans. Geosci. Remote Sens.*, *53*(4), 1985–1996, doi:10.1109/TGRS.2014.2351497.

Budgell, W. P. (2005), Numerical simulation of ice-ocean variability in the Barents Sea region: Towards dynamical downscaling, *Ocean Dyn.*, *55*, 370–387, doi:10.1007/s10236-005-0008-3.

Cavalieri, D., T. Markus, and J. C. Comiso (2014), *AMSR-E/Aqua Daily L3 12.5 km Brightness Temperature, Sea Ice Concentration, & Snow Depth Polar Grids. Version 3 for 2006–2011*, NASA DAAC at the Natl. Snow and Ice Data Center, Boulder, Colo., doi:10.5067/AMSR-E/AE_SI12.003.

Cavalieri, D. J., C. L. Parkinson, P. Gloersen, and H. Zwally (2015), *Sea Ice Concentrations From Nimbus-7 SMMR and DMSP SSM/I-SSMIS Passive Microwave Data, Data From 2006–2013*, NASA DAAC at the Natl. Snow and Ice Data Center, Boulder, Colo., doi:10.5067/8GQ8LZQVL0VL.

Dee, D. P., et al. (2011), The ERA-Interim reanalysis: Configuration and performance of the data assimilation system, *Q. J. R. Meteorol. Soc.*, *137*, 553–597, doi:10.1002/qj.828.

Depoorter, M. A., J. L. Bamber, J. A. Griggs, J. T. Lenaerts, S. R. Ligtenberg, M. R. van den Broeke, and G. Moholdt (2013), Calving fluxes and basal melt rates of Antarctic ice shelves, *Nature*, *502*(7469), 89–92, doi:10.1038/nature12567.

Dinniman, M. S., J. M. Klinck, and W. O. Smith Jr. (2007), Influence of sea ice cover and icebergs on circulation and water mass formation in a numerical circulation model of the Ross Sea, Antarctica, *J. Geophys. Res.*, *112*, C11013, doi:10.1029/2006JC004036.

Dinniman, M. S., J. M. Klinck, and W. O. Smith Jr. (2011), A model study of Circumpolar Deep Water on the west Antarctic Peninsula and Ross Sea continental shelves, *Deep Sea Res., Part II*, *58*, 1508–1523, doi:10.1016/j.dsr2.2010.11.013.

Dutrieux, P., J. De Rydt, A. Jenkins, P. R. Holland, H. K. Ha, S. H. Lee, E. J. Steig, Q. Ding, E. P. Abrahamsen, and M. Schroder (2014), Strong sensitivity of Pine Island ice-shelf melting to climatic variability, *Science*, *343*(174), 174–178, doi:10.1126/science.1244341.

Fairall, C. W., E. F. Bradley, J. E. Hare, A. A. Grachev, and J. B. Edson (2003), Bulk parameterization of air-sea fluxes: Updates and verification for the COARE algorithm, *J. Clim.*, *16*, 571–591.

Fretwell, P., et al. (2013), Bedmap2: Improved ice bed, surface and thickness datasets for Antarctica, *Cryosphere*, *7*, 375–393, doi:10.5194/tc-7-375-2013.

Gwyther, D. E., B. K. Galton-Fenzi, J. R. Hunter, and J. L. Roberts (2014), Simulated melt rates for the Totten and Dalton ice shelves, *Ocean Sci.*, *10*, 267–279, doi:10.5194/os-10-267-2014.

Hedström, K. S. (2009), Technical manual for a coupled sea-ice/ocean circulation model (Version 3), technical report OCS Study MMS 2009-062, Arctic Region Supercomputing Center, Univ. Alaska, Fairbanks. [Available at https://www.myroms.org/wiki/images/3/3b/Manual_2010.pdf.]

Holland, D. M., and A. Jenkins (1999), Modeling thermodynamic ice-ocean interactions at the base of an ice shelf, *J. Phys. Oceanogr.*, *29*, 1787–1800.

Holland, P. R., A. Jenkins, and D. M. Holland (2008), The response of ice shelf basal melting to variations in ocean temperature, *J. Clim.*, *21*, 2558–2572, doi:10.1175/2007JCLI1909.1.

Holland, P. R., A. Jenkins, and D. M. Holland (2010), Ice and ocean processes in the Bellingshausen Sea, Antarctica, *J. Geophys. Res.*, *115*, C05020, doi:10.1029/2008JC005219.

Hunke, E. C., and J. K. Dukowicz (1997), An elastic-viscous-plastic model for sea ice dynamics, *J. Phys. Oceanogr.*, *27*, 1849–1867.

Jacobs, S., A. Jenkins, H. Hellmer, C. Giulivi, F. Nitsche, B. Huber, and R. Guerrero (2012), The Amundsen Sea and the Antarctic Ice Sheet, *Oceanography*, *25*(3), 154–163, doi:10.5670/oceanog.2012.90.

Jacobs, S. S., A. Jenkins, C. F. Giulivi, and P. Dutrieux (2011), Stronger ocean circulation and increased melting under Pine Island Glacier ice shelf, *Nat. Geosci.*, *4*, 519–523, doi:10.1038/ngeo1188.

Joughin, I., B. E. Smith, and B. Medley (2014), Marine ice sheet collapse potentially under way for the Thwaites Glacier Basin, West Antarctica, *Science*, *334*, 735–738, doi:10.1126/science.1249055.

Khazendar, A., M. P. Schodlok, I. Fenty, S. R. Ligtenberg, E. Rignot, and M. R. van den Broeke (2013), Observed thinning of Totten Glacier is linked to coastal polynya variability, *Nat. Commun.*, *4*, 2857, doi:10.1038/ncomms3857.

Large, W. G., J. C. McWilliams, and S. C. Doney (1994), Oceanic vertical mixing: A review and a model with a nonlocal boundary layer parameterization, *Rev. Geophys.*, *32*(4), 363–403.

Little, C. M., A. Gnanadesikan, and M. Oppenheimer (2009), How ice shelf morphology controls basal melting, *J. Geophys. Res.*, *114*, C12007, doi:10.1029/2008JC005197.

Mankoff, K. D., S. S. Jacobs, S. M. Tulaczyk, and S. E. Stammerjohn (2012), The role of Pine Island Glacier ice shelf basal channels in deep-water upwelling, polynyas and ocean circulation in Pine Island Bay, Antarctica, *Ann. Glaciol.*, *53*(60), 123–128, doi:10.3189/2012AoG60A062.

Marchesiello, P., J. C. McWilliams, and A. Shchepetkin (2001), Open boundary conditions for long-term integration of regional oceanic models, *Ocean Modell.*, *3*, 1–20.

Martin, S., R. Drucker, R. Kwok, and B. Holt (2004), Estimation of the thin ice thickness and heat flux for the Chukchi Sea Alaskan coast polynya from Special Sensor Microwave/Imager data, 1990–2001, *J. Geophys. Res.*, *109*, C10012, doi:10.1029/2004JC002428.

Mazloff, M. R., P. Heimbach, and C. Wunsch (2010), An eddy-permitting Southern Ocean state estimate, *J. Phys. Oceanogr.*, *40*(5), 880–889, doi:10.1175/2009jpo4236.1.

Mellor, G. L., and L. Kantha (1989), An ice-ocean coupled model, *J. Geophys. Res.*, *94*, 10,937–10,954.

Mouginot, J., E. Rignot, and B. Scheuchl (2014), Sustained increase in ice discharge from the Amundsen Sea Embayment, West Antarctica, from 1973 to 2013, *Geophys. Res. Lett.*, *41*, 1576–1584, doi:10.1002/2013GL059069.

Naish, T., et al. (2009), Obliquity-paced Pliocene West Antarctic ice sheet oscillations, *Nature*, *458*, 322–329, doi:10.1038/nature07867.

Nakayama, Y., M. Schroder, and H. H. Hellmer (2013), From circumpolar deep water to the glacial meltwater plume on the eastern Amundsen Shelf, *Deep Sea Res., Part I*, *77*, 50–62, doi:10.1016/j.dsr.2013.04.001.

Nowicki, S., et al. (2013), Insights into spatial sensitivities of ice mass response to environmental change from the SeaRISE ice sheet modeling project I: Antarctica, *J. Geophys. Res.*, *118*, 1002–1024, doi:10.1002/jgrf.20081.

Padman, L., et al. (2012), Oceanic controls on the mass balance of Wilkins Ice Shelf, Antarctica, *J. Geophys. Res.*, *117*, C01010, doi:10.1029/2011JC007301.

Pollard, D., and R. M. DeConto (2009), Modelling West Antarctic ice sheet growth and collapse through the past five million years, *Nature*, *458*, 329–333, doi:10.1038/nature07809.

Powers, J. G., K. W. Manning, D. H. Bromwich, J. J. Cassano, and A. M. Cayette (2012), A decade of Antarctic science support through AMPS, *Bull. Am. Meteorol. Soc.*, *93*, 1699–1712, doi:10.1175/bams-d-11-00186.1.

Pritchard, H. D., S. R. Ligtenberg, H. A. Fricker, D. G. Vaughan, M. R. van den Broeke, and L. Padman (2012), Antarctic ice-sheet loss driven by basal melting of ice shelves, *Nature*, *484*, 502–505, doi:10.1038/nature10968.

Rignot, E., S. Jacobs, J. Mouginot, and B. Scheuchl (2013), Ice-shelf melting around Antarctica, *Science*, *341*, 266–270, doi:10.1126/science.1235798.

Rignot, E., J. Mouginot, M. Morlighem, H. Seroussi, and B. Scheuchl (2014), Widespread, rapid grounding line retreat of Pine Island, Thwaites, Smith, and Kohler glaciers, West Antarctica, from 1992 to 2011, *Geophys. Res. Lett.*, *41*, 3502–3509, doi:10.1002/2014gl060140.

Scambos, T., B. Raup, and J. Bohlander (2001), *Images of Antarctic Ice Shelves (Years 2006–2013)*, Natl. Snow and Ice Data Center, Boulder, Colo., doi:10.7265/N5NC5Z4N.

Schodlok, M. P., D. Menemenlis, E. Rignot, and M. Studinger (2012), Sensitivity of the ice-shelf/ocean system to the sub-ice-shelf cavity shape measured by NASA IceBridge in Pine Island Glacier, west Antarctica, *Ann. Glaciol.*, *53*(60), 156–162, doi:10.3189/2012AoG60A073.

Shchepetkin, A. F., and J. C. McWilliams (2005), The Regional Oceanic Modeling System (ROMS): A split-explicit, free-surface, topography-following-coordinate oceanic model, *Ocean Modell.*, *9*, 347–404, doi:10.1016/j.ocemod.2004.08.002.

St-Laurent, P., J. M. Klinck, and M. S. Dinniman (2013), On the role of coastal troughs in the circulation of warm Circumpolar Deep Water on Antarctic Shelves, *J. Phys. Oceanogr.*, *43*(1), 51–64, doi:10.1175/jpo-d-11-0237.1.
Steig, E. J., Q. Ding, D. S. Battisti, and A. Jenkins (2012), Tropical forcing of Circumpolar Deep Water inflow and outlet glacier thinning in the Amundsen Sea embayment, West Antarctica, *Ann. Glaciol.*, *53*(60), 19–28, doi:10.3189/2012AoG60A110.
Thoma, M., A. Jenkins, D. Holland, and S. Jacobs (2008), Modelling Circumpolar Deep Water intrusions on the Amundsen Sea continental shelf, Antarctica, *Geophys. Res. Lett.*, *35*, L18602, doi:10.1029/2008GL034939.
Thurnherr, A. M., S. S. Jacobs, P. Dutrieux, and C. F. Giulivi (2014), Export and circulation of ice cavity water in Pine Island Bay, West Antarctica, *J. Geophys. Res.*, *119*, 1754–1764, doi:10.1002/2013jc009307.
Timmermann, R., et al. (2010), A consistent dataset of Antarctic ice sheet topography, cavity geometry, and global bathymetry, *Earth Syst. Sci. Data Discuss.*, *2*(2), 261–273, doi:10.5194/essdd-2-261-2010.
Timmermann, R., Q. Wang, and H. H. Hellmer (2012), Ice-shelf basal melting in a global finite-element sea-ice/ice-shelf/ocean model, *Ann. Glaciol.*, *53*(60), 303–314, doi:10.3189/2012AoG60A156.
Tinto, K. J., and R. E. Bell (2011), Progressive unpinning of Thwaites Glacier from newly identified offshore ridge: Constraints from aerogravity, *Geophys. Res. Lett.*, *38*, L20503, doi:10.1029/2011GL049026.
Wåhlin, A. K., O. Kalén, L. Arneborg, G. Björk, G. K. Carvajal, H. K. Ha, T. W. Kim, S. H. Lee, J. H. Lee, and C. Stranne (2013), Variability of warm deep water inflow in a submarine trough on the Amundsen Sea shelf, *J. Phys. Oceanogr*, *43*, 2054–2070, doi:10.1175/JPO-D-12-0157.1.